Journal of Materials Chemistry A

PAPER

Cite this: J. Mater. Chem. A, 2015, 3, 3547

Mo-doped LiV_3O_8 nanorod-assembled nanosheets as a high performance cathode material for lithium ion batteries†

Huanqiao Song,*[a] Yaguang Liu,[a] Cuiping Zhang,[a] Chaofeng Liu[a] and Guozhong Cao*[ab]

Mo-doped LiV_3O_8 nanorod-assembled nanosheets were prepared by a simple hydrothermal reaction of $LiOH·H_2O$, V_2O_5 and $(NH_4)_6Mo_7O_{24}$ as precursors followed by thermal annealing. X-ray diffraction results show that the intensity of the (100) peak is less than that of ($\bar{1}11$) in the Mo-doped LiV_3O_8 nanosheets, suggesting the inferior crystallinity of Mo-doped LiV_3O_8. Shifts of Raman bands to lower wavenumbers are found in the Mo-doped LiV_3O_8 material, which when compared with those of pure LiV_3O_8 indicates that Mo^{6+} substitutes V^{5+} in the LiV_3O_8 layer. X-ray photoelectron spectroscopy reveals that the Mo-doped LiV_3O_8 nanosheets calcined at 400 °C contain 25% V^{4+} and 3.5% oxygen vacancies, which likely compensates for the accommodation of 5% Mo^{6+}. The Brunauer–Emmett–Teller surface area of the Mo-doped LiV_3O_8 nanosheets calcined at 400 °C is 24.8 $m^2\ g^{-1}$, which is nearly double of LiV_3O_8 calcined at 400 °C (13.9 $m^2\ g^{-1}$). The electrochemical and lithium ion intercalation properties of both pure and Mo-doped LiV_3O_8 cathode were systematically studied using cyclic voltammetry, chronopotentiometry, and electrochemical impedance spectroscopy. The Mo-doped LiV_3O_8 cathode shows a much higher lithium ion storage capacity, better cyclic stability, and higher rate capability than the pure LiV_3O_8 cathode. The maximum discharge capacity of the Mo-doped LiV_3O_8 (calcined at 400 °C) cathode is 269.0 mA h g^{-1} and retains 205.9 mA h g^{-1} at a current density of 300 mA g^{-1}, which is much higher than 97.8 mA h g^{-1} of the LiV_3O_8 (also calcined at 400 °C) cathode during the 100th cycle. Note that Mo doping is found to increase the electrochemical reaction reversibility, reduce the electrochemical reaction resistance, and enhance the lithium ion diffusivity. The possible reasons for such significant enhancement in the discharge/charge capacity, cyclic stability and rate performance of the Mo-doped LiV_3O_8 cathode are elucidated based on the structure analysis.

Received 20th October 2014
Accepted 12th December 2014

DOI: 10.1039/c4ta05616g

www.rsc.org/MaterialsA

1. Introduction

Lithium-ion battery technology has attracted considerable attention due to the dramatically growing demand for safe, efficient, small sized and cost effective electrical energy storage systems.[1–3] Lithium-ion batteries (LIBs) have been widely used in portable electronic devices, implantable medical devices, and electric vehicles; however, their performances lag far behind the rapidly increasing demands of ever advancing electronic devices. It is imperative to develop new electrode materials and/or improve the existing electrode materials for higher discharge capacity, cycling stability and rate capability. Compared with anode materials, the exploration of cathode materials with higher discharge capacity and cycling stability remains a great challenge for the development of next generation LIBs as their energy storage performances are limited by cathode.[4,5] Among the cathode materials for LIBs, layered monoclinic lithium trivanadate (LiV_3O_8) has gained great interest due to its high specific capacity, low cost, and good safety features.[6–8]

LiV_3O_8 has excellent suitability as an intercalation host, and it consists two basic structural units, VO_6 octahedra and VO_5 distorted trigonal bipyramids, which form two different sites for lithium ions, *i.e.* octahedral and tetrahedral.[9] The VO_6 octahedra form a zigzag double ribbon and the VO_5 bipyramids form another zigzag ribbon similar to the VO_6 double ribbon. The two ribbons are connected through corner-sharing oxygen ions to form a V–O layer. Note that the V–O layers are held together by the pre-existing lithium ions at the octahedral sites;[10] moreover, over three equivalents of lithium ions can intercalate into the tetrahedral sites of LiV_3O_8.[9] Almost all the vanadium components exist in the pentavalent state in the octahedra, and the remaining vanadium components exist in the tetravalent state because of the occupation of the

[a]Beijing Institute of Nanoenergy and Nanosystems, Chinese Academy of Sciences, Beijing 100083, China. E-mail: songhuanqiao@binn.cas.cn; gzcao@u.washington.edu
[b]Department of Materials and Engineering, University of Washington, Seattle, WA 98195-2120, USA

† Electronic supplementary information (ESI) available. See DOI: 10.1039/c4ta05616g

tetrahedral sites by excess lithium ions in the discharge process.[11] The theoretical capacity of LiV_3O_8 with 3 Li intercalations/deintercalations is about 280 mA h g^{-1}, which is much higher than those of the currently used cathode materials,[12–14] making it a highly potential cathode material for next-generation LIBs. However, LiV_3O_8 as a cathode material has relatively low electronic conductivity (approximately 10^{-6} S cm^{-1})[15,16] and a low Li-ion diffusion coefficient (*i.e.*, $\sim 10^{-13}$ cm^2 s^{-1}),[17] both of which significantly limit its electrochemical property and practical applications as a cathode in LIBs. Numerous strategies have been investigated with the aim of improving the electrical conductivity and diffusion coefficient of LiV_3O_8, including the synthesis of different structured materials, metal ion doping, carbon or other conductive material coating, and reducing the particle size to nanometers.[8,18–21] All of these methods have improved the electrochemical properties, including the discharge capacity, rate capacity, and cycle performance, through the reduced transport lengths for both the electrons and Li ions, or increased electrode/electrolyte contact area, or easy accommodation of the strain of Li ion insertion/extraction.[7,18,22–24] However, the comprehensive performance of LiV_3O_8 cathodes need to be further improved for practical applications. For example, Mo *et al.*[8] synthesized LiV_3O_8 nanorods on graphene. The reversible capacity is stable at 251 mA h g^{-1} after 10 cycles at a rate of 100 mA g^{-1}, but its reversible capacity decreases to 98 mA h g^{-1} when the discharge/charge rate is increased to 1500 mA g^{-1}. Hierarchical plate-arrayed LiV_3O_8 as a cathode material for LIBs present a relatively lower discharge capacity of 226.4 mA h g^{-1} at 1/6 C, but they possess a much higher reversible capacity of 111.8 mA h g^{-1} at 10 C.[24]

In this study, we report the synthesis of a Mo-doped LiV_3O_8 (MDLVO) nanorod-assembled nanosheet electrode by a simple hydrothermal reaction, followed by thermal annealing, without any additive. The MDLVO electrodes demonstrated high capacity and excellent rate performance and cycle performance. Various analytical methods, including X-ray diffraction (XRD), thermogravimetric/differential thermal analysis (TGA/DTA), Raman spectroscopy, scanning electron microscopy (SEM), transmission electron microscopy (TEM) and X-ray photoelectron spectroscopy (XPS), were used to investigate the chemical composition, microstructures and morphologies. The electrochemical and lithium ion intercalation properties of both pure and MDLVO cathodes are systematically studied and the correlations between the excellent electrochemical performance and the microstructure of MDLVO are elucidated.

2. Experimental

All the starting materials were of analytically pure grade and were used directly without any purification. Mo-doped LiV_3O_8 nanorod-assembled nanosheets were prepared by a typical hydrothermal synthesis, followed by the thermal annealing method as illustrated in Fig. 1. In the typical synthesis, $(NH_4)_6Mo_7O_{24}$, V_2O_5 and $LiOH{\cdot}H_2O$ were dissolved in distilled water at room temperature with constant stirring. The molar ratio of Li : V : Mo was 1.05 : 2.85 : 0.15 in the solution, and then the mixture was heated at 80 °C for several hours with

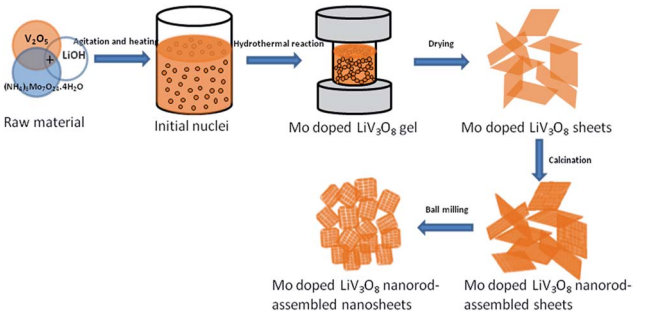

Fig. 1 Schematic illustration of the synthesis route of the Mo-doped LiV_3O_8 nanorod-assembled nanosheets in this study.

vigorous stirring to evaporate the water (2/5 was removed) until a yellow-brown sol was obtained. The sol, exhibiting a pH of ~4, was then transferred into a 100 ml Teflon lined stainless steel autoclave. The autoclave was heated at 180 °C for 48 h and then cooled to room temperature quickly. The MDLVO gel was freeze-dried in order to prevent agglomeration, and further treated at different temperatures (300, 350, 400 and 450 °C) for 2 h in air. The samples were then milled to obtain the MDLVO nanorod-assembled nanosheets, and they were designated MDLVO (300), MDLVO (350), MDLVO (400) and MDLVO (450) according to the calcination temperatures. For comparison, LiV_3O_8 without Mo was also prepared using the same method and calcined at 400 °C for 2 h.

XRD was performed on a Bruker powder diffraction system (model D8 Advanced) with a Cu-Kα radiation source. The 2θ angular regions between 10° and 70° were investigated at a scan rate of 6° min^{-1} with a step of 0.02°. Raman spectra were collected at ± 0.65 cm^{-1} resolution with a Horiba JOBIN YVON Raman system (LabRAM HR Evolution) using an argon ion laser (532 nm) as the excitation source. XPS analysis was conducted on a K-Alpha 1063 instrument using monochromatic Al Kα X-ray source operated at 72 W. Charging effects were corrected by adjusting the binding energy of C 1s to 284.6 eV in the XPS spectra. A non-linear, least-squares algorithm was employed to determine the best fit to each of the V 2P core level spectra with two Gaussian–Lorentzian curves, corresponding to two oxidation states (V^{4+} and V^{5+}). The relative atomic ratio of V^{4+} and V^{5+} was determined from the corresponding area ratios of these fits. The elemental composition of the MDLVO nanosheets was determined using an energy dispersive X-ray spectrometer (OXFORD INCA 300).

The morphology and energy dispersive spectroscopy (EDS) mappings of the as-prepared composite materials were detected by a field emission scanning electron microscope (FE-SEM, SU 8020) at 10 kV. TEM investigations were performed using a JEOL JEM-2010 instrument with an accelerating voltage of 200 kV. N_2 adsorption–desorption analysis was carried out using a Micromeritics ASAP 2020 HD88. The typical sample weight used was about 500 mg. The outgas condition was set to 240 min at 250 °C under vacuum, and all adsorption–desorption measurements were carried out at liquid nitrogen temperature. A combined TGA/DTA instrument (Mettler-Toledo STAR system, TGA/SDTA)

was used to study the decomposition and reaction of the precursors.

The working electrode was prepared by mixing the active material, polyvinylidene fluoride, and Super P conductive carbon in the weight ratio of 70 : 10 : 20. *N*-Methylpyrrolidone was used as the solvent. The resultant slurry was then uniformly cast onto an Al foil current collector and dried overnight at 80 °C. After evaporation of the solvent and heating at 120 °C under vacuum for 12 h, the electrodes were cut into disks and assembled into CR2025 coin type cells in a glove box filled with pure argon gas. Celgard polypropylene was used as the separator, and the electrolyte was 1 M $LiPF_6$ in a mixture of ethylene carbonate and dimethyl carbonate (1 : 1). Li metal was used as the counter electrode and reference electrode. The mass density of the active material in each electrode disk was 2.5–3.5 mg cm^{-2}. The electrochemical performances of the prepared electrodes were characterized with a Land CT2001A tester system at room temperature. The cells were galvanostatically discharged and charged at different current densities within the range of 2.0–4.0 V (*vs.* Li/Li^+). Cyclic voltammetry (CV) tests were carried out using Solartron electrochemical workstation with a scan rate of 0.1 mV s^{-1} at room temperature. The specific capacity and the current density were calculated based on the mass of the active material. Electrochemical impedance spectroscopy (EIS) experiments were performed using the Solartron 1287A in conjunction with a Solartron 1260A impedance analyzer over the frequency range from 100 kHz to 0.01 Hz and the AC amplitude was 10.0 mV. Before the EIS test, the cells were charged to 2.7 V and then kept at that voltage for a period of time to reach a stable state. The electrical conductivities of the prepared samples were measured using the direct current (DC) four-probe technique, as described elsewhere.[25,26] The sample was converted into a pellet at a pressure of 100 MPa, and then the pellet was gold coated, dried and sandwiched between stainless steel blocking electrodes for the electrical conductivity measurements.

3. Results and discussion

Fig. 2 shows the TGA-DTA results of the MDLVO cryogel under flowing air with a ramping rate of 5 °C min^{-1}. In the temperature range between 28 and 165 °C, the gradual weight loss of 9.4% is assigned to the evaporation and removal of NH_3 or water bonded physically to the MDLVO cryogel, corresponding with an evident endothermic peak in the DTA curve. The subsequent weight loss of 3.2% between 165 and 325 °C can be ascribed to the deintercalation of chemically bonded water and the formation of crystalline MDLVO. No appreciable weight loss in the TGA at temperatures above 325 °C was found, which suggests that the removal of chemically bonded water was completed at 325 °C. There is a big and wide exothermic peak in the range of 420–530 °C on the DTA curve but the weight of the sample remains constant, which is likely due to the further crystallization of MDLVO.[27]

The XRD patterns of LiV_3O_8 and the as-prepared MDLVO nanosheets heat-treated at different temperatures (300 °C, 350 °C, 400 °C and 450 °C) are shown in Fig. 3. It can be seen

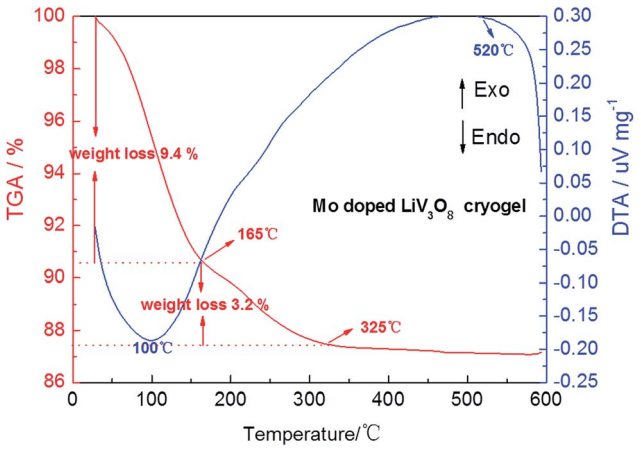

Fig. 2 TGA and DTA results for the Mo-doped LiV_3O_8 cryogel.

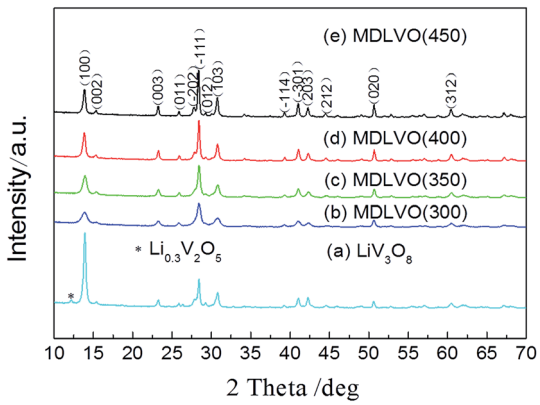

Fig. 3 XRD patterns of LiV_3O_8 calcined at 400 °C and Mo-doped LiV_3O_8 (MDLVO) calcined at different temperatures.

that the MDLVO samples calcined at temperatures between 300 and 450 °C exhibit almost identical XRD patterns, which can be readily indexed into a monoclinic crystalline LiV_3O_8 phase (JCPDS Card no. 72-1193, space group: $P2_1/m$), though the diffraction peak intensity (in curves b–e) changes with the temperature. The diffraction peaks of MDLVO become sharp and narrow when the calcination temperature increased from 300 to 450 °C, indicating that the primary particle grew up with the temperature increase. The average crystallite sizes were calculated from the LiV_3O_8 (312) peak using Scherrer's formula, and they are 9.70 nm for MDLVO (300), 14.31 nm for MDLVO (350), 19.72 nm for MDLVO (400) and 23.96 nm for MDLVO (450). Comparing the patterns of MDLVO with that of pure LiV_3O_8, no crystalline molybdenum or molybdenum oxides were observed in the MDLVO patterns. A small impurity phase of $Li_{0.3}V_2O_5$ was detected at ~12.3° in the pure LiV_3O_8 pattern, but it was not found in the MDLVO patterns. Moreover, it should be noted that the intensity of the (100) peak is less than that of $(\bar{1}11)$ in MDLVO, which is different from the LiV_3O_8 in this study and in the previously reported studies.[28–30] Wang *et al.*[20] ascribed the low intensity of the (100) peak to inferior crystallinity. Evidently, except for these differences, the peak

position and the peak intensities of the pure and doped LiV_3O_8 are similar, which suggests that ion doping does not significantly change the lattice parameter. Raman spectrum is more sensitive to the doping sites and is considered a more suitable method to investigate the doping ions in the LiV_3O_8 crystal lattice. Therefore, we measured the Raman spectra of the pure and doped LiV_3O_8 calcined at 400 °C, and the results are shown in Fig. 4. The Raman band of pure LiV_3O_8 at 994 cm^{-1} is attributed to the vibrational modes belonging to the A_g symmetry, and can be assigned to the V–O stretching vibrations of the VO_5 pyramids,[31] whereas the band at 771 cm^{-1} is probably due to the atomic motions of the corner-sharing oxygen among the VO_6, VO_5, and LiO_6 polyhedra.[31,32] The symmetry stretching modes in MDLVO shift to lower wavenumbers (990 cm^{-1} and 760 cm^{-1}) because the mass of Mo^{6+} (95.94) is greater than that of V^{5+} (50.94). The mode shifts indicate a slight distortion of the crystal cells, which suggests that Mo^{6+} substitutes V^{5+} in the VO_6 octahedra and VO_5 trigonal bipyramids.[33] In addition, it is apparent that the peak strengths at 990 and 760 cm^{-1} for the Mo-doped sample are quite weak compared to those for pure LiV_3O_8. This indicates that the short-range local condition is less ordered and less crystallized in the Mo-doped sample,[31,34] which is consistent with the XRD results.

The XPS spectra give the information about the surface composition and the valence states of the elements. Fig. 5a is the XPS spectrum of MDLVO calcined at 400 °C, in which peaks of Li 1s, V 2p, Mo 3d and O 1s are clearly observed. Fig. 5b and c are the high resolution XPS of Mo 3d and V 2p after fitting, whereas the peaks at 233.09 and 236.18 eV in Fig. 5b correspond to Mo 3d5/2 and Mo 3d3/2, respectively, which agree well with the previously studied values for Mo^{6+} in molybdenum oxide or other molybdates.[35,36] The V 2p spectrum in Fig. 5c shows two main peaks at 517.33 and 524.82 eV, which are ascribed to the spin–orbit splitting of the components V^{5+} 2p3/2 and V^{5+} 2p1/2, respectively.[37] It is noteworthy that the peaks of V^{4+} are also clearly found at 516.23 eV (V^{4+} 2p3/2) and 521.88 eV (V^{4+} 2p1/2),[21] suggesting the formation of low valence state vanadium in the MDLVO nanosheets. The relative atomic ratio of V^{5+} and V^{4+} is calculated based on the peak areas, and the result is 3 : 1, which indicates that the content of V^{4+} is more than the content of Mo^{6+}. In order to compensate for the charge, a lot of oxygen

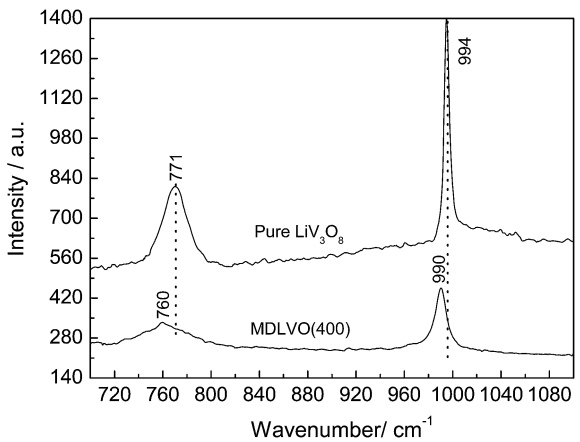

Fig. 4 Raman spectra of pure LiV_3O_8 and Mo-doped LiV_3O_8 (MDLVO) nanorod-assembled nanosheets calcined at 400 °C.

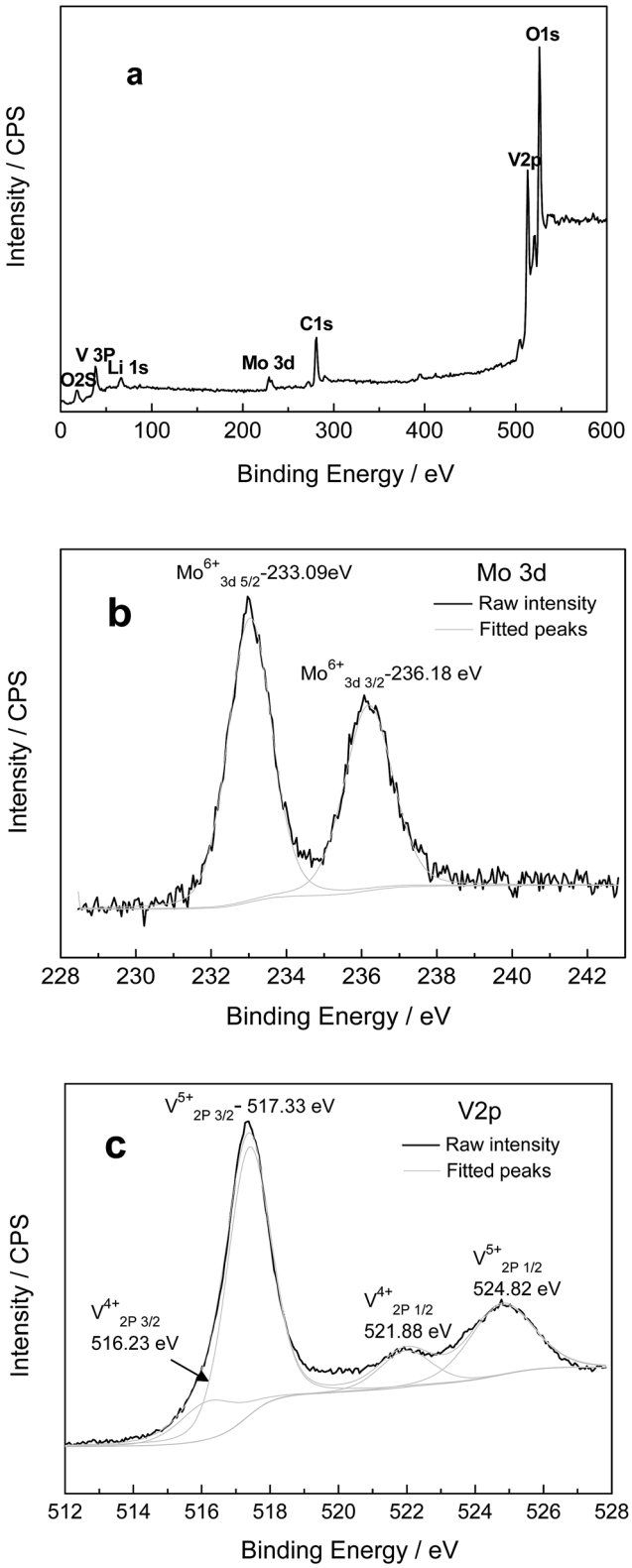

Fig. 5 XPS spectra of Mo-doped LiV_3O_8 calcined at 400 °C: (a) survey spectrum and high-resolution, (b) Mo 3d, (c) V 2p spectra.

vacancies must be created in the lattice of MDLVO. It can be determined that the formula of MDLVO is $LiMo_{0.15}V_{2.85}O_{7.72}(V_O^{\cdot\cdot})_{0.28}$, which is consistent with the results of the elemental composition analysis by EDS measurements. The presence of oxygen vacancies leaves more open void space for easy lithium ion diffusion. In addition, the oxygen vacancies may serve as possible nucleation centers for easy phase transformation during the lithium ion insertion and extraction processes.[38,39] Moreover, the presence of V^{4+} and associated oxygen vacancies can improve the electrical conductivity of the cathode.[40,41] The electrical conductivities of pure LiV_3O_8 and MDLVO (400) measured by the DC four-probe technique are 3.52×10^{-6} S cm^{-1} and 2.89×10^{-5} S cm^{-1}, respectively.

The morphology and structure of MDLVO prepared at 400 °C were characterized by FE-SEM and TEM. As shown in Fig. 6a, nanosheets with average length of 800 nm–1.5 μm and width of 1 μm can be observed from the SEM image. Moreover, it can be found from the close examination in Fig. 6b that the MDLVO (400) nanosheets consist numerous nanobelts, which are 100–200 nm long and 40–60 nm wide (see Fig. 6c and d). The

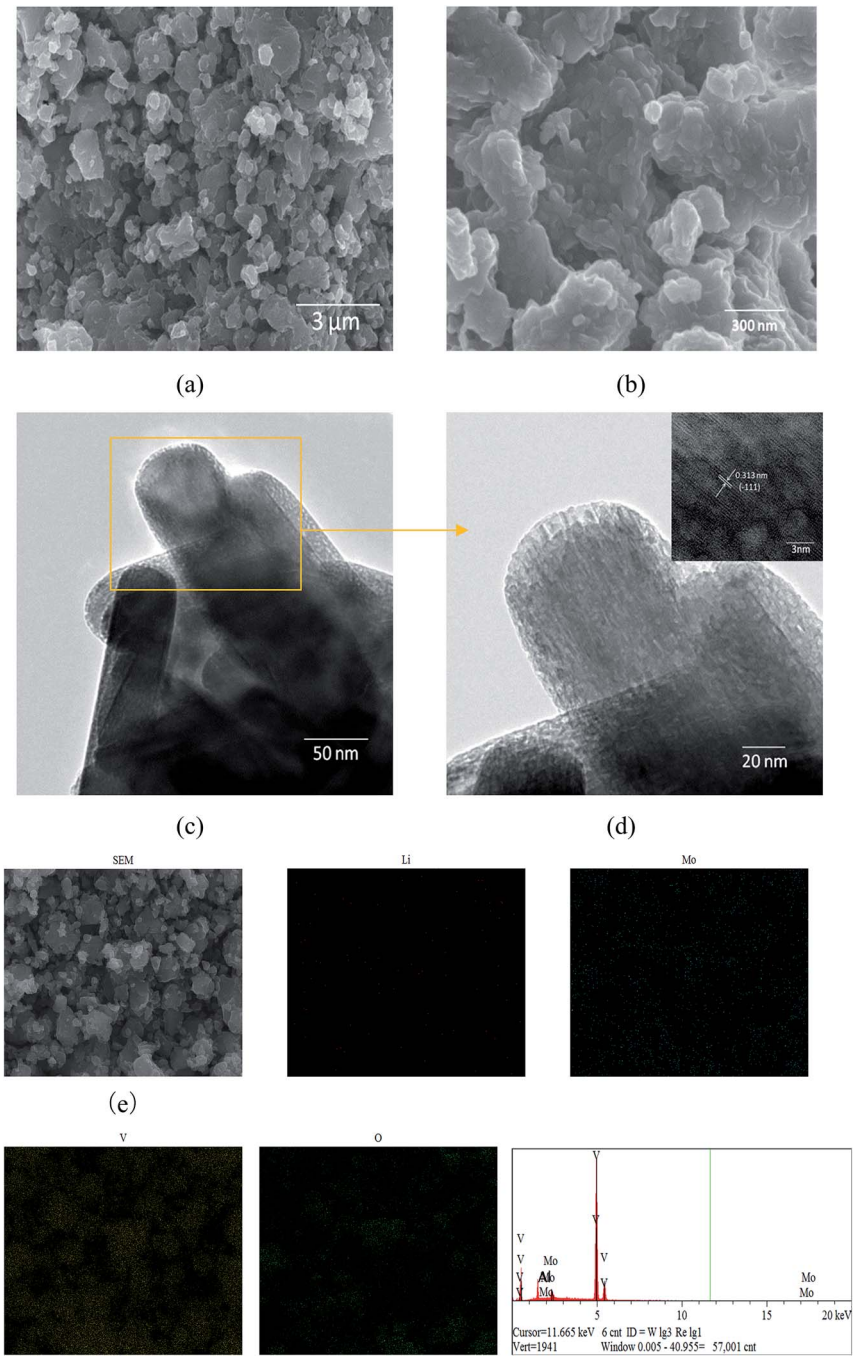

Fig. 6 FE-SEM (a and b), TEM (c and d), high resolution TEM (the inset in d) and SEM images of Mo-doped LiV_3O_8 (400) and its corresponding EDS maps of Li, Mo, V and O elements (e).

composition of MDLVO (400) can be unraveled using the element mapping images of lithium, molybdenum, vanadium and oxygen. It can be seen from Fig. 6e that lithium, molybdenum, vanadium and oxygen distributions are quite uniform; moreover, molybdenum is well distributed overall the LiV_3O_8, further suggesting the entry of molybdenum into the lattice of LiV_3O_8. FE-SEM analyses of the MDLVO cryogel and the products, performed at different temperatures help us to understand the formation of nanorod-assembled nanosheets. Fig. S3a and b† show the image of the MDLVO cryogel. As is shown in the figure, the cryogel is composed of sheet MDLVO assembled by the ribbon-like MDLVO fiber. This structure is similar with the V_2O_5 cryogel or xerogel reported in previous studies.[42,43] In general, V_2O_5 cryogel or xerogel is considered to be of a long-range ordered and local disordered structure,[44] and the XRD result in Fig. S4† presents that the diffraction peaks of MDLVO cryogel were not sharp, which indicates that the structure of MDLVO cryogel is disordered (or amorphous). The cryogel here is developed from the commercially available V_2O_5, LiOH and $(NH_4)_6Mo_7O_{24}$ utilizing additive-free solution processing methods as governed by the following reaction in a stainless steel autoclave:

$$28LiOH + 39.9V_2O_5 + 0.6(NH_4)_6Mo_7O_{24} \xrightarrow{180\ ^\circ C} 28LiMo_{0.15}V_{2.85}O_8 + 15.8H_2O + 3.6NH_3\uparrow + 1.05O_2\uparrow$$

During the hydrothermal reaction, ribbon-like MDLVO fibers are formed in gel. The ribbon-like MDLVO fibers intertwine into the MDLVO sheet during the drying process. The MDLVO cryogel is composed of long nanobelts, which are about 100 nm wide. The morphology of these nanobelts could be related to the formation of hydrous MDLVO, the same as hydrous V_2O_5 in the previous reported studies.[43–45] Similar nanobelts were also observed in $Li_{1.2}V_3O_8$ gel by Xie *et al.*[46] The V_2O_5 gel provides a kind of matrix for the LiV_3O_8 gel, and therefore the LiV_3O_8 or MDLVO gel shows a network structure resembles that of the V_2O_5 gel.[46] The as-prepared samples after calcination show high thermal stability with good retention of the MDLVO sheet structure, which is confirmed by the results of FE-SEM in Fig. S3c and d.† In addition, it can also be seen that some nanorods grew up from the connection parts of the MDLVO nanobelts in Fig. S3d,† indicating that the disordered structure of the MDLVO cryogel transformed into the ordered structure of nanorods. The nanorod-assembled nanosheets were obtained after ball milling, which explains the formation mechanism of the nanorod-assembled nanosheets and that the nanorods grew from the nanosheets with increase in the calcination temperature (see Fig. S3e–h†). Such a nanoscale subunit-assembled nanosheet hierarchical structure (MDLVO (400)) gives rise to a Brunauer–Emmett–Teller (BET) surface area of 24.8 $m^2\ g^{-1}$ (shown in Fig. 7), which is relatively higher than that of LiV_3O_8 (13.9 $m^2\ g^{-1}$) and previous reports.[6,28] The bigger surface area of MDLVO (400) is favorable for fast electrolyte penetration and lithium ion diffusion. The Barrett–Joyner–Halenda (BJH) desorption analyses indicate that the sample contains mesopores with a size peak of 22.4 nm. These appropriate size

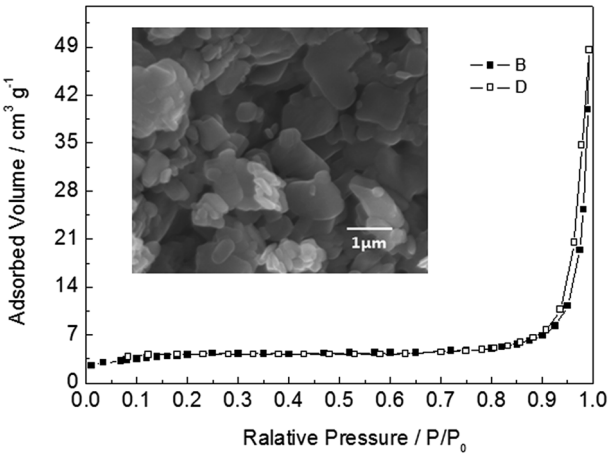

Fig. 7 N_2 adsorption/desorption isotherm and the SEM image (inset) of LiV_3O_8 nanosheets calcined at 400 °C (a), N_2 adsorption/desorption isotherm and the corresponding BJH pore-size distribution curves (inset) of Mo doped LiV_3O_8 nanosheets calcined at 400 °C (b).

mesopores can provide excellent channels and cavities for complete, homogeneous and easy Li^+ intercalation and diffusion in the material.

Fig. 8 shows the second-cycle CV curves for MDLVO (400) and LiV_3O_8 (calcined at 400 °C) electrodes at a scan rate of 0.1 mV s^{-1} over the range of 2.0–4.0 V (*vs.* Li/Li^+). During the cathodic scan of the LiV_3O_8 sample, the peak at ~3.57 V corresponds to the initial Li ion insertion into the octahedral site of the LiV_3O_8 host structure,[17,32] whereas the peak at ~2.72 V belongs to the Li ion insertion in the empty tetrahedral site through a single-phase reaction between $0 < x < 2.0$ in $Li_{1+x}V_3O_8$, and the peak at ~2.39 V is related to the Li ion occupation in the tetrahedral sites accompanied with a two-phase transition from $Li_3V_3O_8$ to $Li_4V_3O_8$ ($2.0 < x < 3.0$).[47–49] The corresponding anodic peaks for LiV_3O_8 at ~3.65 V, ~3.03 V and ~2.55 V are the Li ion extraction reactions. In addition to these peaks, one obvious peak at 3.46 V is observed in the anodic scan. While two peaks at 3.17 and 3.37 V appear in the cathodic scan. These peaks can be ascribed to

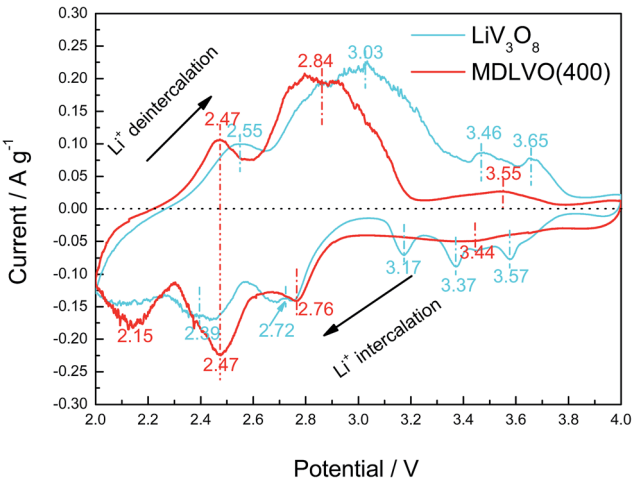

Fig. 8 The second-cycle CV curves for pure LiV_3O_8 calcined at 400 °C and Mo-doped LiV_3O_8 (400) electrodes at a scan rate of 0.1 mV s^{-1} over the range of 2.0–4.0 V (*vs.* Li/Li^+).

the active phase of $Li_{0.3}V_2O_5$ as observed in the XRD result of LiV_3O_8, suggesting the different lithium sites with energy differences for lithium ion holding.[7,50,51] For the MDLVO (400) electrode, the main cathodic peaks shift to ~3.44 V, ~2.76 V and ~2.47 V (as above mentioned, ~3.57 V, ~2.72 V and ~2.39 V for the pure LiV_3O_8 electrode), and the main anodic peaks shift to ~3.55 V, ~2.84 V and ~2.47 V from ~3.65 V, ~3.03 V and ~2.55 V, respectively, for the LiV_3O_8 electrode. The smaller potential intervals of the MDLVO (400) electrodes between the cathodic and anodic peaks indicate an excellent reversible insertion/extraction reaction of the Li ion. The accommodation of Mo^{6+} stabilizes the LiV_3O_8 layer, and therefore benefits the insertion/extraction process of Li ions within the layered LiV_3O_8 structure. Similar results have also been reported for Ce-doped LiV_3O_8 and Si-doped LiV_3O_8.[52,53] In addition, Su *et al.*[54] ascribed the decrease of potential intervals of the oxidation and reduction peaks to the improvement of electronic conductivity after the formation of a carbon coating on $Li_3V_2(PO_4)_3$. For our MDLVO (400) electrode, the presence of mixed-valence V^{4+}/V^{5+} increased the electrical conductivity of cathode materials,[40] and thus decreased the polarization of Li ion insertion/extraction reaction. Moreover, the cathodic peak at ~2.15 V, which is nearly invisible in the CV curve of LiV_3O_8, is attributed to the slower kinetic insertion process of the Li ion where the single-phase transition corresponding to the $Li_4V_3O_8$ takes place ($3.0 < x < 3.2$).[55] As can be seen in the CV curves for the two electrodes, a higher current intensity on the LiV_3O_8 electrode at the cathodic peak of 3.57 V was found and a similar current density with the MDLVO electrode at 2.72 V was detected on the LiV_3O_8 electrode. It is believed that the Li ion diffusion efficiency is high in pure LiV_3O_8 for the initial insertion. A lot of diffusion paths and empty tetrahedral sites are available for the occupation of Li ion between the layers in the earlier stage of Li ion insertion. Therefore, the Li ion insertion can proceed efficiently in pure LiV_3O_8. Pan *et al.*[22] observed a similar phenomenon for the higher current density in bulk LiV_3O_8 than that in the nanorod-like LiV_3O_8 at the early stage of Li ion insertion. However, the peak current density of the pure LiV_3O_8 electrode is much lower than that of the MDLVO (400) electrode for the two-phase transition at 2.39 V. Kawakita *et al.*[49] reported that the Li ion diffusion coefficient in the LiV_3O_8 electrode is much lower for the two-phase transition stage and considered that the insertion becomes kinetic limited at this stage. While for the electrode containing Mo^{6+}, the BET surface area of the material is almost twice that of pure LiV_3O_8; therefore, the required Li ion diffusion distance is effectively shortened. Furthermore, the low crystallinity, quantities of oxygen vacancies and the appropriate pore size distribution can allow easy accommodation of more Li ions during the insertion process, thus lowering the energy barrier for the diffusion process. This also explains the higher current density on MDLVO (400) electrode at 2.15 V during the cathodic scan. During the anodic scan, a similar behavior is observed. All of these differences in the CV curves confirm the improvement of the Li ion insertion/extraction kinetics in the MDLVO (400) cathode.

Fig. 9 shows the discharge/charge curves and cyclic performance of the pure LiV_3O_8 calcined at 400 °C and MDLVO (400) at a current density of 300 mA g^{-1}. As can be seen in Fig. 9a, a rapid voltage decrease during discharge and a quick voltage

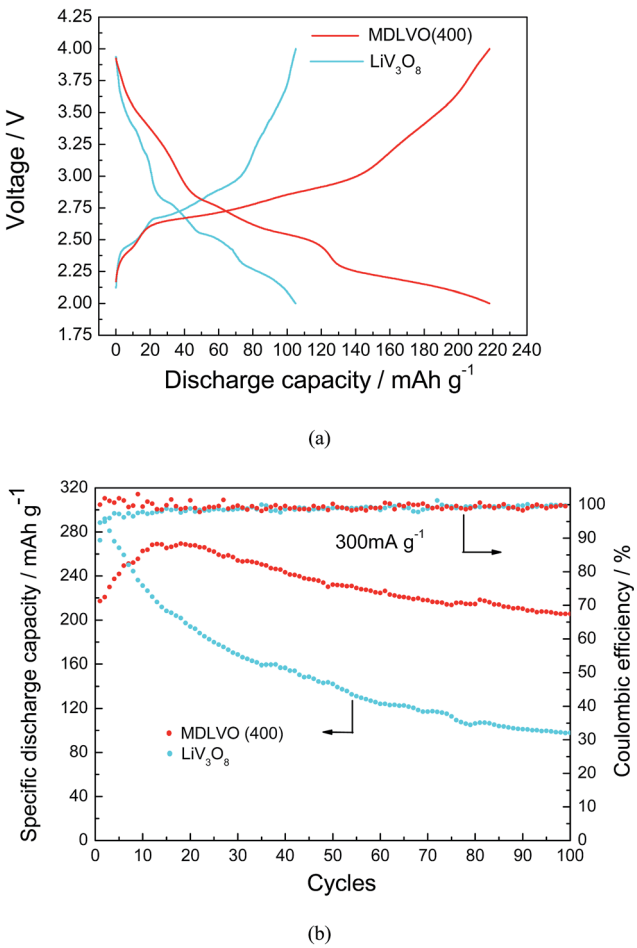

Fig. 9 Discharge/charge curves (a) and cyclic performance (b) of pure LiV_3O_8 and Mo-doped LiV_3O_8 calcined at 400 °C at a current density of 300 mA g^{-1}.

increase during charge were observed in the voltage range between 4 V and 2.8 V for the pure LiV_3O_8 electrode, followed by three short plateaus from 2.8 V to 2 V, which indicates the multistep processes and a negligible capacity was obtained in this voltage range. The overall specific discharge capacity was only 105.0 mA h g^{-1}. However, as can be seen in Fig. 9a, the MDLVO (400) nanorod-assembled nanosheet electrode had more evident plateaus and higher specific discharge capacity. When the discharge capacities were more stable, it delivered a specific capacity of 218.2 mA h g^{-1} during the 81st cycle, which is almost twice the capacity of the pure LiV_3O_8 electrode. Jouanneau *et al.*[56] reported that the particle size and shape greatly influences the insertion rate of the Li ion for crystalline $Li_{1+x}V_3O_8$, and the crystal shape (well-formed crystal or no crystal shape) plays a major role on the cyclability. In our case, the uniform MDLVO (400) nanorod-assembled nanosheets with appropriate crystallinity have larger BET surface area and better mesopore space between the particles (shown in Fig. 7). This MDLVO cathode exhibits both better utilization of the active material and higher capacity than pure LiV_3O_8. Fig. 9b shows the cyclic performance of the pure LiV_3O_8 and MDLVO (400) electrode. The pure LiV_3O_8 electrode delivered an initial specific discharge capacity of 275.0 mA h g^{-1}, and its capacity reached 292.0 mA h g^{-1} during the second cycle; however, it sharply decreased to 192.1 mA h g^{-1} at the 20th cycle and further decreased to 97.8 mA h g^{-1} at the 100th cycle. Such a result is in a good agreement with the previously reported studies,[34,57,58] which widely report a quick capacity loss in the initial cycles for pure LiV_3O_8. Wang *et al.*[59] reported $Li_{1.5}V_3O_8$ nanosheets with an initial capacity of 204 mA h g^{-1} at a current density of 175 mA g^{-1}, but it decreased to 100 mA h g^{-1} after 100 cycles. Guo *et al.*[60] reported LiV_3O_8 with an initial capacity of 248.5 mA h g^{-1} at 300 mA g^{-1}; however, the capacity faded to 105.2 mA h g^{-1} rapidly during the first 50 cycles. The capacity fading may result from the irreversible phase transition between LiV_3O_8 and $Li_4V_3O_8$[61] or the deterioration of the crystal structure and the dissolution of a small amount of V^{III} in the electrolyte.[62] For our MDLVO (400) electrode, the specific capacity and cycle stability were significantly enhanced, although it delivered an initial discharge capacity of 217.1 mA h g^{-1} at the current density of 300 mA g^{-1}. The discharge capacity steadily increased to 269.0 mA h g^{-1} during the 13th cycle, which is equivalent to 2.9 mol Li per mol of LiV_3O_8. Then, the specific discharge capacity slightly decreased to 230.2 mA h g^{-1} during the 49th cycle and became quite stable in the subsequent cycles (only 0.47% and 0.25% capacity fading per cycle between cycles 49 and 100 and cycles 49 and 150, respectively). Feng *et al.*[21] found that the B doped LiV_3O_8 had a higher discharge capacity and stability than pure LiV_3O_8. They ascribed the good performance to the broader pathway between adjacent vanadate chains for the diffusion of lithium in the material and the more stable layer structure after B doping. Ren *et al.*[19] improved the electrochemical performance of LiV_3O_8 by Zr doping. They considered that the Zr substitution for V in LiV_3O_8 increased the interlayer spacing of the bulk material and made it more stable during the discharge/charge cyclings. In the present study, the substitutional doping of Mo^{6+} also increased the interlayer spacing of LiV_3O_8 and stabilized its structure, which leads to the decrease of the irreversible phase transition between LiV_3O_8 and $Li_4V_3O_8$ during the discharge/charge processes. Moreover, the slower activation process of MDLVO (400) nanorod-assembled nanosheet electrode compared with the pure LiV_3O_8 electrode is very similar to the previous report on a V_2O_5 xerogel electrode.[63] For example, N_2-annealed V_2O_5 xerogel electrode presented a low initial discharge capacity of 68 mA h g^{-1}, but it increased to 158 mA h g^{-1} during the 24th cycle, which was ascribed to the surface defect layer on the N_2-annealed V_2O_5 xerogel. In contrast, the air-annealed V_2O_5 xerogel electrode started with a high discharge capacity of 152 mA h g^{-1}, but the capacity decreased sharply in the later cycles and the discharge capacity was only 44 mA h g^{-1} at the 50th cycle. The introduced surface and bulk defects, by doping, result in a much slower activation and more stable cyclic performance for the MDLVO (400) electrode. Therefore, the MDLVO (400) electrode demonstrates a high reversibility for the Li ion insertion/extraction reaction and a stable discharge/charge performance. MDLVO (400) electrode retained a high specific discharge capacity of 205.9 mA h g^{-1} even after 100 cycles, which is still twice the capacity of the pure LiV_3O_8 electrode.

In order to better understand the electrochemical performance of the MDLVO (400) electrode, the cycle performances at increasing current densities from 100 mA g^{-1} to 1500 mA g^{-1} were determined and shown in Fig. 10. For comparison, the testing results of LiV_3O_8 (calcined at 400 °C) electrode are also listed in Fig. 10. As shown in Fig. 10a, the discharge capacity of MDLVO (400) electrode measured in the voltage from 4.0 V to 2.0 V was 331.3 mA h g^{-1} at the current density of 100 mA g^{-1} and remained at 124.5 mA h g^{-1} even at the current density of 1500 mA g^{-1}. This rate capability is much higher than that of the LiV_3O_8 electrode, which is 200.1 mA h g^{-1} at 100 mA g^{-1} and 82.6 mA h g^{-1} at 1500 mA g^{-1}. The capacities were fairly stable at each current density for the MDLVO (400) electrode and even the cell experienced more than 60 cycles at various high current densities. A capacity of 304.8 mA h g^{-1} was obtained when the current density returned to 100 mA g^{-1}, which corresponds to 3.27 mol Li per mol of MDLVO (400). Fig. 10b presents the discharge/charge curves of MDLVO (400) at various current densities. With increase in current density, the decrease of the discharge plateaus and the increase of the charge plateaus were observed, which is attributed to the increasing polarization effect. The capacity and stability could return the initial value after discharge and charge at high current density, indicating the high reversibility of the Li ion insertion/extraction. Gao *et al.*[64] considered that Mo doping is an effective way to improve the structural stability and rate performance of Li_2MnO_3 cathode materials by improving electron/Li-ion transport and oxygen stability. In our sample, V^{4+} and oxygen vacancies appeared in LiV_3O_8 due to the Mo^{6+} doping, which are helpful for improving the electron/Li-ion transport, and the appropriate crystallinity and lattice distortion were found in MDLVO structure, which are favorable to increase the discharge/charge capacity and structural stability of LiV_3O_8. Thus, the MDLVO (400) electrode presents a higher rate performance and better stability than the LiV_3O_8 electrode. The influence of Mo doping

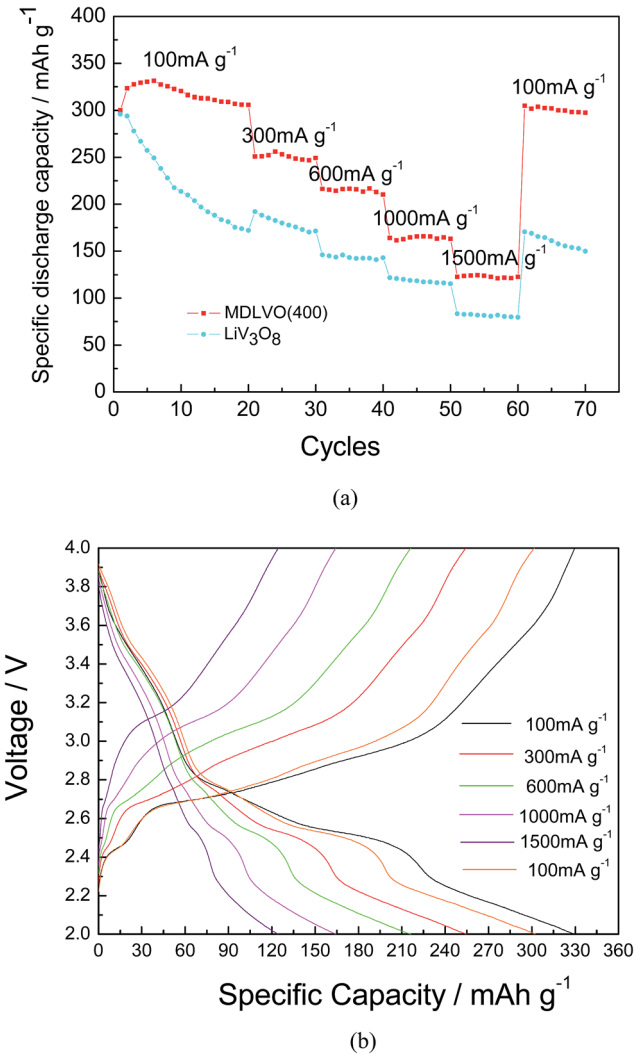

Fig. 10 (a) Discharge capacities of pure LiV_3O_8 calcined at 400 °C and Mo-doped LiV_3O_8 (400) electrodes at various current densities and (b) discharge/charge curves of Mo-doped LiV_3O_8 (400) electrode at various current densities.

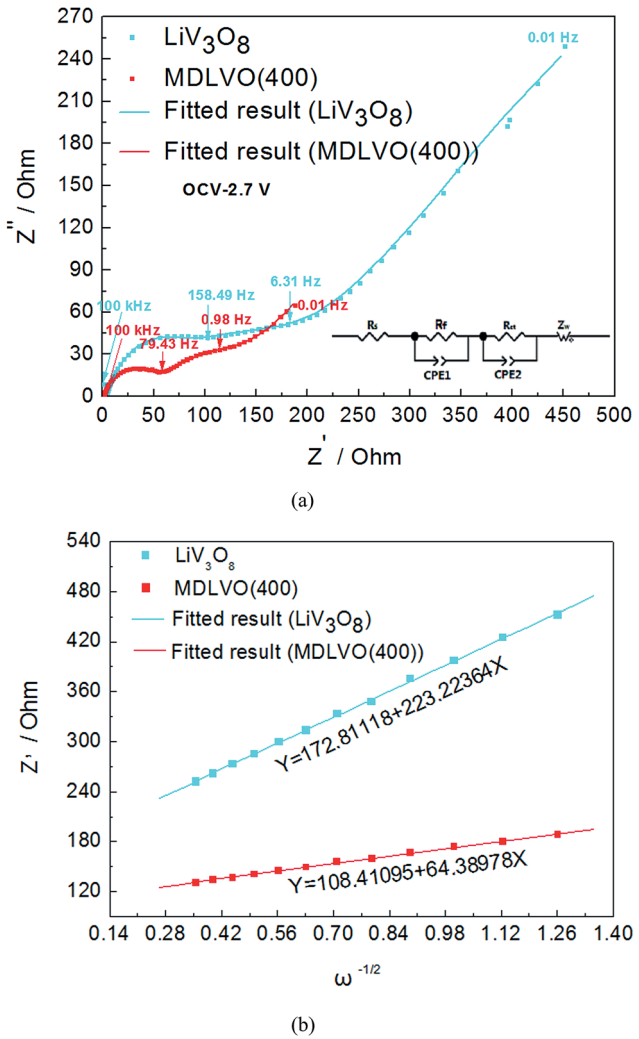

Fig. 11 (a) Nyquist plots of LiV_3O_8 calcined at 400 °C and Mo-doped LiV_3O_8 (400) electrodes at 2.7 V and (b) the relationship curves between Z' and $\omega^{-1/2}$ in the low frequency range.

on the rate capabilities is further verified by the comparison of the EIS results of the activated MDLVO (400) with the LiV_3O_8 electrodes. Fig. 11a shows the Nyquist plots of the MDLVO (400) and LiV_3O_8 electrodes. The Nyquist plots exhibit two semicircles in the high frequency and medium frequency region. The high frequency semicircle is always related to the interface parameters such as surface film contribution, porous nature of electrode, and/or the bulk of materials. The mediate semicircle is attributed to the charge-transfer resistance (R_{ct}),[65,66] and the slope line represents the Warburg impedance (Z_W) at low frequency, which indicates the diffusion of Li ions in the solid matrix. Fitting the curves with the equivalent electrical circuit model, the symbols, R_s, R_f, R_{ct} and Z_W, denote the solution resistance, contact resistance, charge-transfer resistance and Warburg impedance, respectively. The fitting results of R_s, R_f, and R_{ct} of LiV_3O_8 and MDLVO (400) electrodes are shown in Table S1.† It can be seen that the R_f and R_{ct} values of MDLVO (400) electrode are 59.6 Ω and 68.1 Ω, respectively, which are smaller than those of the pure LiV_3O_8 electrode (134.2 Ω and 155.2 Ω), suggesting that the doping of Mo significantly suppresses the increase in both the surface film resistance and charge transfer resistance. It is clearly evident that the MDLVO (400) electrode possesses higher electrical conductivity and the faster charge-transfer reaction for lithium ion insertion and extraction than the pure LiV_3O_8 electrode, further confirming the high efficient doping of Mo into LiV_3O_8. The Li ion diffusion coefficient could be calculated from the low frequency plots based on the following eqn (1) and (2).

$$Z' = R_e + R_{ct} + \sigma_w \omega^{-1/2} \quad (1)$$

$$D_{Li^+} = \frac{R^2T^2}{2A^2n^4F^4C^2\sigma_W{}^2} \quad (2)$$

In eqn (1), $\omega(2\pi f)$ is the angular frequency in the low frequency region, and both R_e and R_{ct} are kinetics parameters independent of frequency, which can be obtained from the

fitting results of Nyquist plots in Fig. 11a. Then, the Warburg coefficient (σ_w) can be obtained from the slope of the fitting line while Z' has a linear relationship with $\omega^{-1/2}$. In eqn (2), R is the gas constant, T is the temperature, A is the area of the electrode, n is the number of electrons transfer per mole of the active material involved in the electrode reaction, F is Faraday's constant, and C is the molar concentration of Li ions. Based on the fitting linear equation in Fig. 11b, the Li ion diffusion coefficients of LiV_3O_8 and MDLVO (400) were calculated and the results are 2.37×10^{-13} cm^2 s^{-1} and 5.74×10^{-12} cm^2 s^{-1}, respectively. The lower surface film and charge transfer resistance and higher Li ion diffusion coefficient and electrical conductivity of MDLVO electrode lead to its superior rate capabilities and other electrochemical properties.

Fig. 12 shows the cyclic stabilities of MDLVO electrodes calcined at different temperatures at a current density of 300 mA g^{-1}. The initial discharge capacities of the MDLVO electrodes calcined at 300, 350, 400 and 450 °C were 254.7, 226.0, 217.1 and 195.8 mA h g^{-1}, respectively. The samples calcined at 300 and 350 °C reached their maximum discharge capacities of 303.1 and 284.6 mA h g^{-1} during the 8th cycle, showing a higher initial storage capacity and a quicker capacity increase in the samples calcined at lower temperatures, and then declined monotonically to 123.0 and 141.9 mA h g^{-1}, respectively, during the 100th cycle. This poor cycling stability can be attributable to the inferior crystallinity and its unstable structure,[56] although the inferior crystallinity could accommodate more lithium ions at their initial stage.[62,67] The cyclic stability was seen to improve in general, as the calcination temperature increased. However, the discharge capacity of MDLVO (400) electrode was higher than that of MDLVO (450) electrode during all the 100 cycles. MDLVO (400) electrode reached its maximum capacity of 269.0 mA h g^{-1} at the 13th cycle, which is much higher than that of the MDLVO (450) electrode (198.7 mA h g^{-1} at the 3rd cycle) and those reported in the previously reported studies.[1,27] The specific discharge capacity of the MDLVO (400) electrode was found to retain 205.9 mA h g^{-1} after 100 cycles (a capacity fading rate of only 0.05% per cycle for the initial 100 cycles), whereas the discharge capacity of MDLVO (450) electrode retained only 163.3 mA h g^{-1} at the 100th cycle (the capacity fading rate is 0.17% per cycle for the 100 cycles). The excellent capacity and cyclic stability of MDLVO (400) electrode likely resulted from the particle size and the aggregation. It can be seen that in Fig. 6 and S3,† the nanorods and the nanosheets are well separated in MDLVO (400), and this structure allowed good accessibility of the electrolyte to the active material. However, in MDLVO (450), the merged and grown nanorods led to a decrease in the void space available for electrolyte diffusion, which agrees well with the decrease of the BET surface area from MDLVO (400) (24.8 m^2 g^{-1}) to MDLVO (450) (16.9 m^2 g^{-1}) in Table S2.† Therefore, the Mo-doped sample calcined at 400 °C possesses the best electrochemical performance.

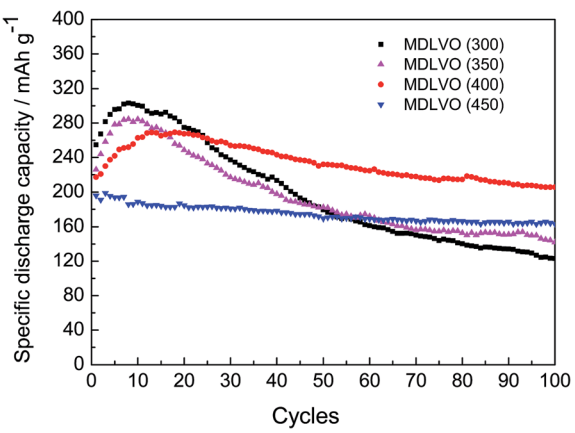

Fig. 12 Cyclic stabilities of Mo-doped LiV_3O_8 electrodes calcined at different temperatures at a current density of 300 mA g^{-1}.

The nanosized material is believed to be favorable with a shortened Li ion diffusion distance and more active sites for electrochemical reactions. Recent studies show that the capacity is enhanced by improving the transport properties of nanostructured LiV_3O_8;[22,27,68] however, the poor rate capability is still a problem.[22] The present MDLVO material exhibits not only a very high capacity and good cycling stability, but also an excellent rate performance. A comparison of the electrochemical performance of our MDLVO with some representative reported LiV_3O_8 electrode materials is given in Table S3.† The outstanding electrochemical performance of MDLVO can be attributed to its higher electrochemical reversibility, higher lithium ion diffusion coefficients and lower electrochemical reaction resistance. Based on the structure analysis, the occupancy of Mo^{6+} could lead to a more stable structure. Jouanneau *et al.*[61,62] reported that the lattice parameter of LiV_3O_8 changes greatly after lithiation during the charge and discharge cycles. A contraction of the *a* lattice parameter and an expansion of the *b* and *c* lattice parameter appear from LiV_3O_8 to $Li_4V_3O_8$ at 2.6 V. Thus, capacity fading occurs due to the damage of the crystal structure caused by the abrupt change in the cell-lattice constant. The substitutional doping of Mo^{6+} into LiV_3O_8 decreases this structural change and improves the electrochemical cycle reversibility. The MDLVO with a nanorod-assembled sheet structure has a bigger BET surface area than pure LiV_3O_8. It has been known that limitation factor for rate capability is the delivery of lithium ions to the surface rather than bulk diffusion when particles are considered in nano dimensions.[69,70] Therefore, the increase of specific surface area is advantageous for electrolyte penetration and fast lithium ion diffusion. Moreover, the presence of oxygen vacancies and V^{4+} in MDLVO structure not only result in the formation of a more open structure and possible nucleation centers for phase transformation during the Li^+ insertion and extraction processes, but also improve the conductivity of the cathode and consequently lead to the much higher capacity and rate performance of the MDLVO electrode.

4. Conclusions

Mo-doped LiV_3O_8 nanorod-assembled nanosheets were successfully synthesized by a facile hydrothermal reaction, followed by thermal annealing without any additives. Nanorods were formed on the surface of MDLVO nanosheets after the heat

treatment. Raman band shifts to lower wavenumbers confirmed the occurrence of lattice distortion in MDLVO material, which proves that Mo^{6+} substitutes V^{5+} in the LiV_3O_8 layer. This substitutional doping is considered to increase the stability of the crystal structure during the lithium ion insertion/extraction processes and be the reason of good cycling stability. The XPS results indicated that V^{4+} and oxygen vacancies appeared in the MDLVO material, which result in the formation of a more open structure and high electronic conductivity of cathode material. The BET surface area of MDLVO (400) increased about 78% compared with pure LiV_3O_8 calcined at 400 °C. The higher BET surface area is favorable for fast electrolyte penetration and lithium ion diffusion. The appropriate pore size distribution (the peak of pore size is 22.4 nm calculated by the BJH method) in MDLVO (400) nanosheets can provide excellent channels and cavities for complete, homogeneous and easy Li^+ intercalation and diffusion. All of these lead to high capacity and rate capability of MDLVO (400). Therefore, the MDLVO (400) nanorod-assembled nanosheets display significantly improved capacity and much better cycling stability and rate capability.

Acknowledgements

This work was supported by the "thousands talents" program for pioneer researcher and his innovation team, China. This work was also supported by the National Science Foundation of China (51374029), Program for New Century Excellent Talents in University (NCET-13-0668).

References

1 J. Lee, A. Urban, X. Li, D. Su, G. Hautier and G. Ceder, *Science*, 2014, **343**, 519–522.
2 B. Guo, X. Yu, X. G. Sun, M. Chi, Z. A. Qiao, J. Liu, Y. S. Hu, X. Q. Yang, J. B. Goodenough and S. Dai, *Energy Environ. Sci.*, 2014, **7**, 2220–2226.
3 S. Y. Lee, K. H. Choi, W. S. Choi, Y. H. Kwon, H. R. Jung, H. C. Shin and J. Y. Kim, *Energy Environ. Sci.*, 2013, **6**, 2414–2423.
4 D. Liu and G. Cao, *Energy Environ. Sci.*, 2010, **3**, 1218–1237.
5 S. T. Myung, K. Amine and Y. K. Sun, *J. Mater. Chem.*, 2010, **20**, 7074–7095.
6 Y. Q. Qiao, X. L. Wang, J. P. Zhou, J. Zhang, C. D. Gu and J. P. Tu, *J. Power Sources*, 2012, **198**, 287–293.
7 S. Huang, J. P. Tu, X. M. Jian, Y. Lu, S. J. Shi, X. Y. Zhao, T. Q. Wang, X. L. Wang and C. D. Gu, *J. Power Sources*, 2014, **245**, 698–705.
8 R. Mo, Y. Du, N. Zhang, D. Rooney and K. Sun, *Chem. Commun.*, 2013, **49**, 9143–9145.
9 L. A. Depicciotto, K. T. Adendorff, D. C. Liles and M. M. Thackeray, *Solid State Ionics*, 1993, **62**, 297–307.
10 A. D. Wadsley, *Acta Crystallogr.*, 1957, **10**, 261–267.
11 J. Kawakita, T. Miura and T. Kishi, *Solid State Ionics*, 1999, **118**, 141–147.
12 Y. Mizuno, E. Hosono, T. Saito, M. Okubo, D. Nishio-Hamane, K. Oh-ishi, T. Kudo and H. Zhou, *J. Phys. Chem. C*, 2012, **116**, 10774–10780.
13 J. Proell, H. Kim, A. Pique, H. J. Seifert and W. Pfleging, *J. Power Sources*, 2014, **255**, 116–124.
14 Y. Zhao, L. Peng, B. Liu and G. Yu, *Nano Lett.*, 2014, **14**, 2849–2853.
15 R. Ramaraghavulu, K. Sivaiah and S. Buddhudu, *Ferroelectrics*, 2012, **432**, 55–64.
16 M. Onoda, *J. Phys.: Condens. Matter*, 2004, **16**, 8957–8969.
17 S. Sarkar, H. Banda and S. Mitra, *Electrochim. Acta*, 2013, **99**, 242–252.
18 D. Sun, G. Jin, H. Wang, X. Huang, Y. Ren, J. Jiang, H. He and Y. Tang, *J. Mater. Chem. A*, 2014, **2**, 8009–8016.
19 X. Ren, S. Hu, C. Shi, P. Zhang, Q. Yuan and J. Liu, *J. Solid State Electrochem.*, 2012, **16**, 2135–2141.
20 H. Wang, Y. Ren, Y. Wang, W. Wang and S. Liu, *CrystEngComm*, 2012, **14**, 2831–2836.
21 Y. Feng, Y. Li and F. Hou, *J. Power Sources*, 2009, **187**, 224–228.
22 A. Pan, J. Liu, J. G. Zhang, G. Cao, W. Xu, Z. Nie, X. Jie, D. Choi, B. W. Arey, C. Wang and S. Liang, *J. Mater. Chem.*, 2011, **21**, 1153–1161.
23 P. Mei, X. L. Wu, H. Xie, L. Sun, Y. Zeng, J. Zhang, L. Tai, X. Guo, L. Cong, S. Ma, C. Yao and R. Wang, *RSC Adv.*, 2014, **4**, 25494–25501.
24 S. Huang, Y. Lu, T. Q. Wang, C. D. Gu, X. L. Wang and J. P. Tu, *J. Power Sources*, 2013, **235**, 256–264.
25 P. Samarasingha, D. H. Tran-Nguyen, M. Behm and A. Wijayasinghe, *Electrochim. Acta*, 2008, **53**, 7995–8000.
26 A. Wijayasinghe, B. Bergman and C. Lagergren, *Solid State Ionics*, 2006, **177**, 165–173.
27 D. Wang, L. Cao, J. Huang and J. Wu, *Ceram. Int.*, 2012, **38**, 2647–2652.
28 H. Liu, Y. Wang, K. Wang, Y. Wang and H. Zhou, *J. Power Sources*, 2009, **192**, 668–673.
29 J. Liu, W. Liu, Y. Wan, S. Ji, J. Wang and Y. Zhou, *RSC Adv.*, 2012, **2**, 10470–10474.
30 H. Liu, Y. Wang, W. Yang and H. Zhou, *Electrochim. Acta*, 2011, **56**, 1392–1398.
31 X. Zhang and R. Frech, *Electrochim. Acta*, 1998, **43**, 861–868.
32 A. Pan, J. G. Zhang, G. Cao, S. Liang, C. Wang, Z. Nie, B. W. Arey, W. Xu, D. Liu, J. Xiao, G. Li and J. Liu, *J. Mater. Chem.*, 2011, **21**, 10077–10084.
33 F. Haass, A. H. Adams, T. Buhrmester, G. Schimanke, M. Martin and H. Fuess, *Phys. Chem. Chem. Phys.*, 2003, **5**, 4317–4324.
34 G. Yang, G. Wang and W. H. Hou, *J. Phys. Chem. B*, 2005, **109**, 11186–11196.
35 L. Si, Z. Yuan, J. Liang, L. Hu, Y. Zhu and Y. Qian, *J. Mater. Chem. A*, 2014, **2**, 9784–9791.
36 P. Qin, G. Fang, W. Ke, F. Cheng, Q. Zheng, J. Wan, H. Lei and X. Zhao, *J. Mater. Chem. A*, 2014, **2**, 2742–2756.
37 G. A. Sawatzky and D. Post, *Phys. Rev. B: Condens. Matter Mater. Phys.*, 1979, **20**, 1546–1555.
38 Y. Zhang, P. Xiao, X. Zhou, D. Liu, B. B. Garcia and G. Cao, *J. Mater. Chem.*, 2009, **19**, 948–953.
39 Y. Li, J. Yao, E. Uchaker, M. Zhang, J. Tian, X. Liu and G. Cao, *J. Phys. Chem. C*, 2013, **117**, 23507–23514.
40 P. Gomez-Romero, *Adv. Mater.*, 2001, **13**, 163–174.

41 I. Boyano, M. Bengoechea, I. de Meatza, O. Miguel, I. Cantero, E. Ochoteco, J. Rodriguez, M. Lira-Cantu and P. Gomez-Romero, *J. Power Sources*, 2007, **166**, 471–477.
42 J. Zhu, L. Cao, Y. Wu, Y. Gong, Z. Liu, H. E. Hoster, Y. Zhang, S. Zhang, S. Yang, Q. Yan, P. M. Ajayan and R. Vajtai, *Nano Lett.*, 2013, **13**, 5408–5413.
43 Y. Li, J. Yao, E. Uchaker, J. Yang, Y. Huang, M. Zhang and G. Cao, *Adv. Eng. Mater.*, 2013, **3**, 1171–1175.
44 V. Petkov, P. N. Trikalitis, E. S. Bozin, S. J. L. Billinge, T. Vogt and M. G. Kanatzidis, *J. Am. Chem. Soc.*, 2002, **124**, 10157–10162.
45 J. Livage, *Chem. Mater.*, 1991, **3**, 578–593.
46 J. G. Xie, J. X. Li, H. Zhan and Y. H. Zhou, *Mater. Lett.*, 2003, **57**, 2682–2687.
47 X. Xu, Y. Z. Luo, L. Q. Mai, Y. L. Zhao, Q. Y. An, L. Xu, F. Hu, L. Zhang and Q. J. Zhang, *NPG Asia Mater.*, 2012, **4**, e20.
48 J. Kawakita, Y. Katayama, T. Miura and T. Kishi, *Solid State Ionics*, 1998, **107**, 145–152.
49 J. Kawakita, T. Miura and T. Kishi, *J. Power Sources*, 1999, **83**, 79–83.
50 J. Kawakita, M. Majima, T. Miura and T. Kishi, *J. Power Sources*, 1997, **66**, 135–139.
51 S. Caes, J. C. Arrebola, N. Krins, P. Eloy, E. M. Gaigneaux, C. Henrist, R. Cloots and B. Vertruyen, *J. Mater. Chem. A*, 2014, **2**, 5809–5815.
52 M. Zhao, L. F. Jiao, H. T. Yuan, Y. Feng and M. Zhang, *Solid State Ionics*, 2007, **178**, 387–391.
53 Z. J. Wu and Y. Zhou, *J. Power Sources*, 2012, **199**, 300–307.
54 J. Su, X. L. Wu, J. S. Lee, J. Kim and Y. G. Guo, *J. Mater. Chem. A*, 2013, **1**, 2508–2514.
55 A. Sakunthala, M. V. Reddy, S. Selvasekarapandian, B. V. R. Chowdari and P. C. Selvin, *J. Phys. Chem. C*, 2010, **114**, 8099–8107.
56 S. Jouanneau, A. Verbaere, S. Lascaud and D. Guyomard, *Solid State Ionics*, 2006, **177**, 311–315.
57 S. H. Ju and Y. C. Kang, *Electrochim. Acta*, 2010, **55**, 6088–6092.
58 D. Wang, L. Cao, J. Huang and J. Wu, *Ceram. Int.*, 2013, **39**, 3759–3764.
59 Y. Wang, X. Xu, C. Cao, C. Shi, W. Mo and H. Zhu, *J. Power Sources*, 2013, **242**, 230–235.
60 H. Guo, L. Liu, H. Shu, X. Yang, Z. Yang, M. Zhou, J. Tan, Z. Yan, H. Hu and X. Wang, *J. Power Sources*, 2014, **247**, 117–126.
61 S. Jouanneau, A. L. La Salle, A. Verbaere, M. Deschamps, S. Lascaud and D. Guyomard, *J. Mater. Chem.*, 2003, **13**, 921–927.
62 S. Jouanneau, A. L. La Salle, A. Verbaere and D. Guyomard, *J. Electrochem. Soc.*, 2005, **152**, A1660–A1667.
63 D. Liu, Y. Liu, A. Pan, K. P. Nagle, G. T. Seidler, Y. H. Jeong and G. Cao, *J. Phys. Chem. C*, 2011, **115**, 4959–4965.
64 Y. Gao, J. Ma, X. Wang, X. Lu, Y. Bai, Z. Wang and L. Chen, *J. Mater. Chem. A*, 2014, **2**, 4811–4818.
65 H. Wang, K. Huang, Y. Ren, X. Huang, S. Liu and W. Wang, *J. Power Sources*, 2011, **196**, 9786–9791.
66 Y. J. Kang, J. H. Kim, S. W. Lee and Y. K. Sun, *Electrochim. Acta*, 2005, **50**, 4784–4791.
67 H. Wang, W. Wang, Y. Ren, K. Huang and S. Liu, *J. Power Sources*, 2012, **199**, 263–269.
68 R. Mo, Y. Du, N. Zhang, D. Rooney and K. Sun, *J. Power Sources*, 2014, **257**, 319–324.
69 B. Kang and G. Ceder, *Nature*, 2009, **458**, 190–193.
70 Q. Shi, J. Liu, R. Hu, M. Zeng, M. Dai and M. Zhu, *RSC Adv.*, 2012, **2**, 7273–7278.

